

Spin and orbital mechanisms of the magneto-gyrotropic photogalvanic effects in GaAs/AlGaAs quantum well structures

V. Lechner,¹ L.E. Golub,² F. Lomakina,¹ V.V. Bel'kov,² P. Olbrich,¹ S. Stachel,¹ I. Caspers,¹ M. Griesbeck,¹ M. Kugler,¹ M.J. Hirmer,¹ T. Korn,¹ C. Schüller,¹ D. Schuh,¹ W. Wegscheider,³ and S.D. Ganichev¹

¹*Terahertz Center, University of Regensburg, 93040 Regensburg, Germany*

²*Ioffe Physical-Technical Institute, Russian Academy of Sciences, 194021 St. Petersburg, Russia and*

³*ETH Zurich, 8093 Zurich, Switzerland*

We report on the study of the linear and circular magneto-gyrotropic photogalvanic effect (MPGE) in GaAs/AlGaAs quantum well structures. Using the fact that in such structures the Landé-factor g^* depends on the quantum well (QW) width and has different signs for narrow and wide QWs, we succeeded to separate spin and orbital contributions to both MPGEs. Our experiments show that, for most quantum well widths, the MPGEs are mainly driven by spin-related mechanisms, which results in a photocurrent proportional to the g^* factor. In structures with a vanishingly small g^* factor, however, linear and circular MPGE are also detected, proving the existence of orbital mechanisms.

PACS numbers: 73.21.Fg, 72.25.Fe, 78.67.De, 73.63.Hs

I. INTRODUCTION

Spin and orbital mechanisms, which are present simultaneously in various physical phenomena, result in two competitive contributions in the observable effects. Textbook examples therefore are Pauli paramagnetism and Landau diamagnetism that yield two comparable contributions to the magnetic susceptibility of an electron gas.¹ Another bright manifestation is the fine structure of exciton lines in a magnetic field.² In all these cases, the electron systems are affected by a magnetic field in two different ways: Via Zeeman splitting of spin sublevels and due to cyclotron twisting of electron trajectories. An interplay of spin and orbital mechanisms is also expected for linear and circular magneto-gyrotropic photogalvanic effects (MPGE). The spin-related mechanisms of both MPGEs were widely discussed in the past and are driven by the spin-dependent relaxation of a non-equilibrium electron gas in gyrotropic two-dimensional electron systems (2DES) (for reviews see Refs. 3–8). The microscopic mechanisms of the spin-driven MPGEs are based on spin-orbit coupling in 2DES with structure and bulk inversion asymmetry (SIA and BIA). In the case of the linear MPGE the absorption of linearly polarized or unpolarized radiation leads to electron gas heating. Due to a spin-dependent energy relaxation of these heated electrons, two equal and oppositely directed electron flows in the spin-up and spin-down subbands result, what represents a pure spin current.^{7–11} The Zeeman splitting of the subbands induced by the in-plane magnetic field leads to the conversion of a spin flow into a measurable spin-polarized electric current. The circular MPGE yields a photocurrent, proportional to the radiation helicity. It is caused by the spin-galvanic effect (SGE),^{12,13} in which the spin-flip relaxation of a spin-polarized non-equilibrium electron gas results in an electric current.^{7,8,14} Here, an in-plane magnetic field rotates the optically induced spin polarization into the plane of

the 2DES due to the Larmor precession. This provides an in-plane spin component, which is necessary for the SGE in (001)-grown QWs. While the spin-based origin of the MPGE was intensively discussed, most recently it was pointed out that orbital effects, caused by a magnetic-field-induced scattering asymmetry, may substantially contribute to the MPGE^{15,16} and thus complicate the analysis of the spin currents. The latter is of importance for the exploration of spin generation and spin-related transport in 2DES, which are major and still growing fields in solid-state research.^{3,17–19}

Here we report on experiments, which allow us to distinguish unambiguously between the spin-dependent and orbital origin of the MPGE by investigating the qualitative difference in their behavior upon a variation of the g^* factor. We use the fact that the electric current resulting from the spin-related roots is proportional to the Zeeman band spin splitting in contrast to the one due to orbital mechanisms. To explore this difference, we utilize the well known fact that in GaAs based quantum wells the Zeeman splitting changes its sign at a certain QW width.^{20–22} This inversion is mostly caused by the opposite signs of the g^* factor in the GaAs with respect to the AlGaAs-barrier and the fact that for narrow QWs the electron wave function deeply penetrates into the barrier. Therefore, we studied the MPGE in a set of structures with QW widths varying from 4 to 30 nm.

The paper is organized as follows. In Sec. II we describe details of the sample preparation and present an overview of the experimental techniques used to study the MPGE. In Sec. III we give an account on combined photoluminescence (PL) and PL excitation (PLE) measurements as well as time-resolved Kerr rotation (TRKR) experiments performed on the sample series in order to determine the electron confinement energies and the electron g^* factor, respectively. Sections IV and V deal with the experimental study and analysis of the linear and circular MPGE, respectively. Finally, we summarize the study.

II. SAMPLES AND EXPERIMENTAL TECHNIQUES

The experiments were carried out on (001)-oriented Si- δ -doped n -type GaAs/Al_{0.3}Ga_{0.7}As structures grown by molecular-beam epitaxy at typical temperatures in excess of 600°C. A set of structures with the same doping profile but different QW widths L_{QW} , between 4 nm and 30 nm, was grown. Figure 1 sketches the conduction band edge of the multiple QW structures together with the corresponding δ -doping positions, and Table I gives the sample parameters. The doping layers are asymmetrically shifted by two different spacer layer thicknesses, l and r , with respect to the QW. In addition, in all samples, except A, the sum $(l+r+L_{\text{QW}})$ was kept constant. The impurities' Coulomb field yields an asymmetric potential profile inside the QWs causing SIA. The investigated samples were square shaped ($5 \times 5 \text{ mm}^2$) and its edges oriented along the $[1\bar{1}0]$ and $[110]$ crystallographic directions. For photocurrent measurements, ohmic contacts were alloyed on the sample corners allowing to probe the photocurrent along the $x \parallel [100]$ and $y \parallel [010]$ crystal axes.

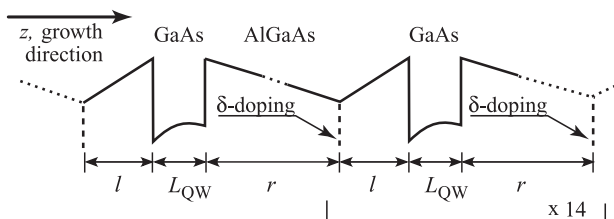


FIG. 1: Conduction band structure of the samples.

The MPGE is measured at room temperature by exciting the samples with linearly or circularly polarized terahertz (THz) laser radiation under normal incidence. As radiation source we used an optically pumped

NH₃ molecular laser^{5,23} operating at a wavelength λ of 280 μm . The wavelength of 280 μm (photon energy of 4.2 meV) was chosen to cause free carrier absorption only. The laser provided single pulses with a pulse duration of about 100 ns and a peak power P of about 6 kW. The photocurrent \mathbf{J} is measured via the voltage drop across a 50 Ω load resistor with a digital oscilloscope. To study the linear MPGE we applied linearly polarized radiation with the radiation field $\mathbf{E} \parallel x$, and an external in-plane magnetic field of B_y of ± 1 T. The resulting current is measured along the x -direction, normally to the magnetic field, B_y . To excite the circular MPGE we used elliptically polarized radiation obtained by a crystal quartz quarter-wave plate. The helicity of the radiation was varied by the rotation of the plate according to $P_{\text{circ}} = \sin 2\varphi$, where φ is the angle between the initial plane of polarization and the optical axis of the $\lambda/4$ -plate. In this case the photocurrent J_x is measured in the direction parallel to B_x . The experimental geometries with $J_x \perp B_y$ for linear and $J_x \parallel B_x$ for the circular MPGE are chosen to probe the currents solely caused by the structure inversion asymmetry.^{24,25} This allows us to reduce the influence of the QW width on the degree of asymmetry. For any other configuration we would also obtain a BIA-induced MPGE, which complicates the data analysis, because BIA itself strongly depends on L_{QW} .²⁶

III. SAMPLE CHARACTERIZATION BY PL AND TRKR TECHNIQUES

A. Experimental technique

To study Landé factors and spin dynamics we used the time-resolved Kerr rotation and photoluminescence techniques, applying a pulsed Ti-Sapphire laser system.

TABLE I: Sample Parameters. Carrier density n_s (per QW-layer), mobility μ , momentum scattering time τ_p calculated from the mobility, measured g^* factor and energy difference ΔE between the transitions (e2hh2)-(e1hh1) are given for $T = 4.2$ K. Also listed: Carrier density $n_s(\text{RT})$ (per QW-layer) and mobility $\mu(\text{RT})$ measured at room temperature.

Sample	L_{QW} [nm]	Spacer l [nm]	Spacer r [nm]	$\chi = \frac{l-r}{l+r}$	n_s $10^{11} [\frac{1}{\text{cm}^2}]$	μ $10^5 [\frac{\text{cm}^2}{\text{Vs}}]$	τ_p [ps]	g^*	ΔE [meV]	$n_s(\text{RT})$ $10^{11} [\frac{1}{\text{cm}^2}]$	$\mu(\text{RT})$ $10^3 [\frac{\text{cm}^2}{\text{Vs}}]$
A	4	45	140	-0.51	1.17	0.509	1.9	0.13	-	1.4	4.8
B	6	74.5	119.5	-0.23	0.874	0.925	3.5	0.106	-	1.3	5.5
C	8.2	73.4	118.4	-0.23	1.11	1.23	4.7	-0.06	-	1.3	6.6
D	10	72.5	117.5	-0.24	1.09	4.95	18.8	-0.157	116	1.3	7.4
E	15	70	115	-0.24	1.26	3.47	13.2	-0.29	59	1.4	8.0
F	20	67.5	112.5	-0.25	1.19	0.642	2.4	-0.337	47	1.2	8.0
G	30	62.5	107.5	-0.26	1.17	12.6	47.9	-0.394	48	1.2	8.2

It generates pulses with a spectral linewidth of about 3-4 meV and a duration of about 600 fs. The central wavelength of the laser is tuned to excite electron-hole pairs at the Fermi energy of the two-dimensional electron gas in the samples. The pulse train from the laser system is split into the pump beam, which is circularly polarized, and the weaker, linearly polarized probe beam. Both beams are focused onto the sample surface at near-normal incidence by an achromat, and the Kerr rotation angle of the reflected probe beam is measured using an optical bridge detector. The typical power density used in the experiments was about 40 W/cm² for the pump beam, and 4 W/cm² for the probe beam. A lock-in scheme is used to increase the sensitivity of the experiment. The samples were mounted in the ³He insert of an optical cryostat and cooled by ³He gas to a nominal temperature of 4.5 K. Magnetic fields of up to 10 Tesla were applied in the sample plane during the TRKR measurements.

For photoluminescence measurements, the Ti-Sapphire laser operated in cw mode and was tuned to higher energies to excite the samples nonresonantly. The excitation density for PL measurements was about 4 W/cm². The PL emitted from the samples was collected using a grating spectrometer and a charge-coupled device (CCD) sensor. All PL measurements were performed without applied magnetic fields at a nominal sample temperature of 4.5 K. For PLE measurements, a tunable cw Ti-Sapphire laser system was used. The PL intensity of the low-energetic flank of the sample was recorded using the spectrometer and the CCD sensor as a function of the laser energy of the Ti-Sapphire laser.

B. Combined PL and PL excitation experiments

To determine the electron confinement energies in the QWs, we performed combined PL and PLE measurements on the sample series. Figure 2(a) shows PL and PLE spectra measured on sample E (15 nm wide QW). The PL spectrum shows a single peak corresponding to the (e1-hh1) transition in the QW. In the PLE spectrum, the onset of absorption at the Fermi energy of the two-dimensional electron system in the QW is clearly visible slightly above this PL peak. The pronounced maximum in the PLE spectrum, indicated by the arrow, corresponds to the (e2-hh2) transition. Due to the increasing confinement in the narrower QWs, the PL peak position shifts to higher energies, as Fig. 2(b) demonstrates. The energy difference between (e1-hh1) and (e2-hh2) transitions as a function of the QW width, shown in Fig. 2(c), and listed in Table I, is extracted from the PL and PLE measurements. It also increases as the QW width is reduced. For QWs, which are thinner than 10 nm, the (e2-hh2) transition lies outside of the tuning range of the Ti-Sapphire laser.

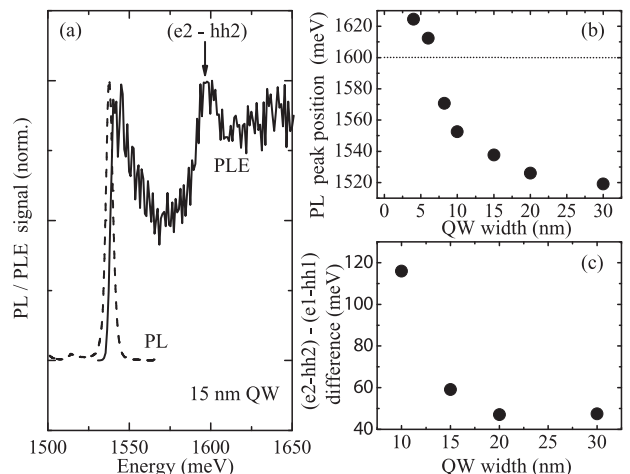


FIG. 2: (a) PL (black dashed line) and PLE (red solid line) spectra of sample E (15 nm wide QW). The arrow indicates the transition energy of the (e2-hh2) transition observed in the PLE spectrum. (b) PL peak energy as a function of the QW width. The dotted line indicates the transition energy for which the electron g^* factor changes its sign.²² (c) Energy difference between (e1-hh1) and (e2-hh2) transitions as a function of the QW width.

C. Time-resolved Kerr rotation experiments

TRKR measurements are used to determine the electron g^* factor in our sample series. It is well-established²⁰ that in GaAs/AlGaAs QWs the electron g^* factor depends on the QW width, and even changes its sign from negative to positive values as a function of the QW thickness. Two effects contribute to this dependence: The conduction band of GaAs is nonparabolic, and the g^* factor of an electron depends on its energy relative to the conduction band edge.²² Additionally, in narrow QWs, the electron wave function has a sizeable amplitude within the AlGaAs barriers, leading to an effective admixture of the (positive) g^* factor in the barrier material to that (negative) of the electron confined in the GaAs QW. In our TRKR measurements, we clearly observe this width dependence [see Fig. 3(a)]. The TRKR traces for different samples, measured at the same magnetic field of 4 T, show the damped Larmor precession of the optically oriented electron spin polarization about the applied magnetic field. The precession frequencies are markedly different: For the widest sample, the precession frequency is high, it decreases for narrower QWs, then increases again for the most narrow sample. The Larmor precession frequencies were determined for all samples by measuring TRKR traces in magnetic fields between 1 and 10 Tesla, and the amplitude of the g^* factor was calculated using a linear fit to the dispersion. Figure 3(b) gives the QW width dependence of the g^* factors in our samples. From TRKR measurements, the sign of the g^* factor is not immediately apparent, although it can be determined using slight modifications

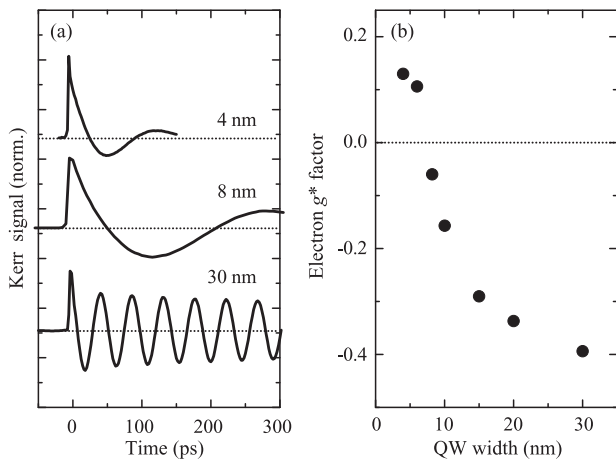


FIG. 3: (a) TRKR traces measured on 3 different samples ($L_{\text{QW}} = 4, 8$ and 30 nm) with an applied in-plane magnetic field of 4 Tesla. (b) Electron g^* factor as a function of the QW width extracted from the TRKR data. The sign of the g^* factor, which cannot be directly extracted from the TRKR traces, has been inferred from the PL transition energies.

of a typical TRKR setup and rigorous data analysis.²⁷ Here, we infer the sign of the g^* factor from the PL transition energies observed for our samples. In their studies on the g^* factor's dependence on the QW width, Yugova et al.²² observed the zero crossing of the g^* factor for a fundamental transition energy (e1-hh1) of 1600 meV (indicated by the dotted line in Fig. 2(b)). In sample C, we observe the PL peak at 1572 meV, well below the value for zero crossing, and in the thinner sample B the PL peak is at 1616 meV, well above the value for zero crossing. Hence, we assign negative g^* factor values to the samples with nominal QW widths between 30 nm and 8.2 nm, and positive g^* factors to the two thinnest samples. The TRKR measurements also allow us to study the dependence of the spin dephasing time (SDT), T_2^* , on the QW width. Figure 4(a) shows a series of TRKR traces measured on different samples without applied magnetic fields. No simple correlation between the QW width and the SDT is apparent, as evidenced by the SDT data given in Fig. 4(b) (note the logarithmic scale for the SDT). In all samples, the dominant spin dephasing mechanism at low temperatures is the D'yakonov-Perel mechanism²⁸, and in the motional narrowing regime, the SDT is given by

$$\frac{1}{T_2^*} = \Omega^2 \tau_p, \quad (1)$$

where τ_p is the momentum relaxation time, and Ω is the precession frequency due to the effective spin-orbit fields. As the QW width is reduced, the magnitude of the Dresselhaus field increases due to the momentum quantization along the growth axis, and the magnitude of the Rashba field was also shown to increase monotonously with decreasing QW width in the thickness range investigated here.²⁹ The rising amplitude of both spin-orbit

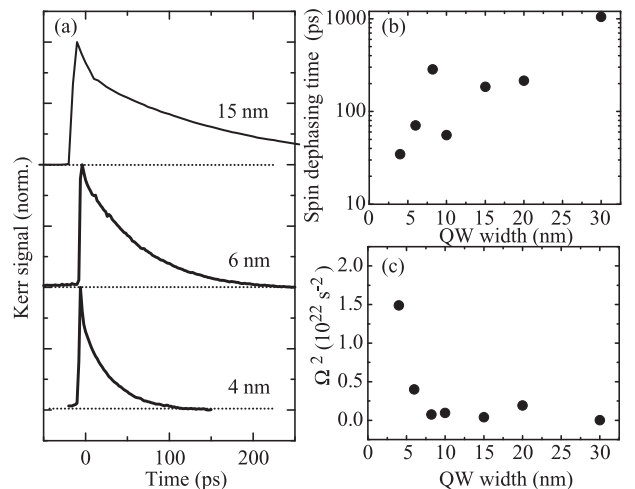


FIG. 4: (a) Zero-field TRKR traces measured on three different samples with $L_{\text{QW}} = 4, 6$ and 15 nm. (b) Zero-field SDT as a function of the QW width (log. scale). (c) Ω^2 as a function of the QW width.

fields should lead to a more rapid dephasing in thinner QWs according to Eq. (1). We can explain the non-monotonous dependence of the SDT on the QW width by taking into account the different momentum relaxation times in our samples. The momentum relaxation times τ_p , calculated from the mobility data measured at 4.2 K, are listed in Table I. Using these values, we calculate Ω^2 using Eq. (1). The results, shown in Fig. 4(c), demonstrate a near-monotonous increase of Ω^2 with decreasing QW width, as expected from the QW width dependence of the effective spin-orbit fields.

IV. LINEAR MPGE

The linear MPGE excited by linearly polarized radiation has been detected in all samples. Under THz irradiation we observed a photocurrent signal J_x , which is linearly increasing with rising magnetic field strength B_y and changes its sign upon the inversion of the magnetic field direction from $B_y > 0$ to $B_y < 0$, demonstrating the typical MPGE behavior. As our experiments here are focused on the linear MPGE, we eliminate any possible background in our experiments by

$$\mathbf{J}^L = [\mathbf{J}(B_y) - \mathbf{J}(-B_y)]/2. \quad (2)$$

Figure 5 shows the photocurrent \mathbf{J}^L as a function of L_{QW} obtained for magnetic fields of ± 1 T. For comparison the effective Landé factor g^* , extracted from the time-resolved Kerr rotation, is also plotted (details of these measurements are already discussed in Sec. III). As an important result Fig. 5 demonstrates that the SIA-induced photocurrent J_x , similarly to the g^* factor, changes its sign upon the variation of L_{QW} .³⁰ However, there is a difference in the zero points: While the g^* factor equals to zero at $L_{\text{QW}} \sim 6.5$ nm, the current vanishes

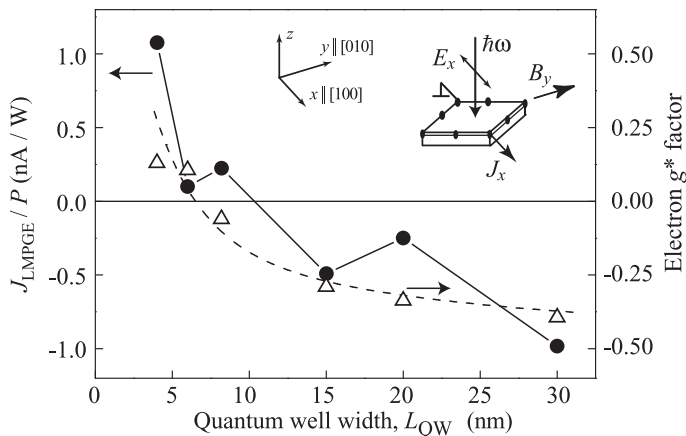


FIG. 5: Dependence of the linear MPGE (circles) on L_{QW} obtained at room temperature, $B_y = \pm 1$ T and photon energy $\hbar\omega = 4.4$ meV and corresponding g^* factors (triangles, by TRKR). The inset shows the experimental geometry for the LMPGE.

for $L_{\text{QW}} \sim 10$ nm. It will be shown below that this shift between the inversion points as well as the MPGE's sign inversion can be well described by the interplay of spin and orbital mechanisms in the current formation.

To explain qualitatively our results we describe the basic physics of these mechanisms. We start with the spin-related mechanism. The generation of a spin-polarized current due to the MPGE may be discussed in the frame of a recently proposed model for the spin-dependent asymmetric energy relaxation of a non-equilibrium electron gas heated by, e.g., THz or microwave radiation.^{10,31} Free electrons are excited to higher energy states by absorbing radiation and then relax into an equilibrium state by emitting phonons. Figure 6 sketches the hot electron energy relaxation processes in the two spin subbands ($s_y = \pm 1/2$) that are split due to the Zeeman effect in the presence of an external magnetic field. The electron relaxation from higher to lower energies is shown by bent arrows. In gyrotropic media, like GaAs low-dimensional semiconductors, the spin-orbit interaction makes the scattering probability spin-dependent:¹⁰

$$W_{\mathbf{k}'\mathbf{k}} = W_0 \{1 + \xi [\boldsymbol{\sigma} \times (\mathbf{k} + \mathbf{k}')]_z\}, \quad (3)$$

where W_0 is the symmetric part of the scattering probability, which determines the mobility (we consider SIA only). Here \mathbf{k} and \mathbf{k}' are the initial and scattered electron wave vectors and $\boldsymbol{\sigma}$ is the vector composed of the Pauli matrices. Thus, the electron transitions to positive and negative k'_x -states occur with different probabilities causing an imbalance in the distribution of carriers in both subbands between positive and negative k_x -states. This is shown by different thicknesses of the bent arrows in Fig. 6. At zero magnetic field the asymmetry of the electron-phonon interaction would lead to a spin current, but not an electric current: This is due to the fact that the oppositely directed electron fluxes, $i_{\pm 1/2} \propto \xi$, are of equal strength and therefore, compensate each other.

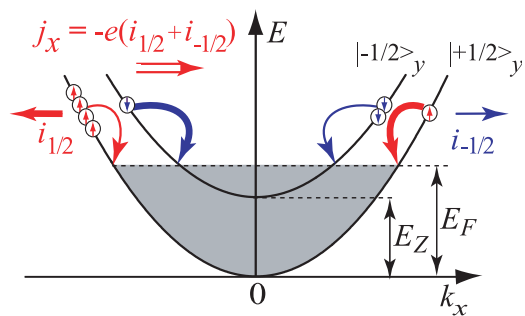


FIG. 6: Spin based model for the linear MPGE. See details in the text.

The presence of an in-plane magnetic field B_y , however, leads to the Zeeman splitting of the $s_y = \pm 1/2$ subbands. As a consequence, the electron densities $n_{+1/2}$ and $n_{-1/2}$ in both spin subbands become different, and the fluxes $i_{\pm 1/2}$ do not longer compensate each other and therefore a net electric current results. Obviously, this current, classified as linear MPGE, is spin-polarized and its value is proportional to the Zeeman spin splitting induced by the magnetic field. Its QW width dependence is described by the product $g^* \xi$.

In order to estimate the parameter ξ caused by SIA, we take into account that the remote impurities create an electric field \mathcal{E} along the growth direction, leading to the asymmetry of the QW. Therefore, the eigenstates in this structure are superpositions of the states of the rectangular QW. As a result, the envelope wave functions in the first and second subbands of size quantization $\phi_{1,2}(z)$ are given by

$$\begin{aligned} \phi_1(z) &= \varphi_1(z) + \frac{e\mathcal{E}z_{21}}{E_{21}}\varphi_2(z), \\ \phi_2(z) &= \varphi_2(z) - \frac{e\mathcal{E}z_{21}}{E_{21}}\varphi_1(z). \end{aligned} \quad (4)$$

Here z is the growth direction, $\varphi_{1,2}(z)$ are the functions of size quantization in the ground and the first excited subbands of the rectangular QW of width L_{QW} , E_{21} is the energy separation between these subbands, and z_{21} is the coordinate matrix element calculated between these states. This leads to $\xi(L_{\text{QW}}) \sim z_{21}/E_{21}$, and to the following dependence of this contribution to the linear MPGE current:

$$j_{\text{spin}}^{\text{L}}(L_{\text{QW}}) \sim g^*(L_{\text{QW}}) \frac{z_{21}}{E_{21}}. \quad (5)$$

Here we disregard a weak dependence of the scattering probability on the QW width.

In a set of samples with similar structure inversion asymmetry, like in our samples, where SIA is controlled by the asymmetric doping, the MPGE should vanish for the sample with zero g^* factor and change its sign upon a QW width variation. Thus, the spin-related mechanism of the MPGE describes well the appearance of the sign inversion. However, it can not explain the fact

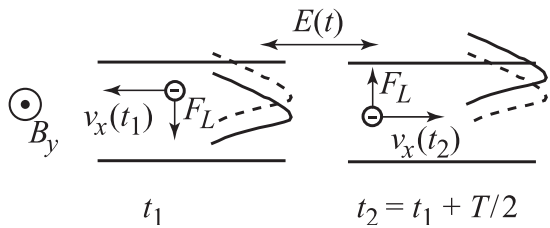


FIG. 7: Orbital model for the linear MPGE. Solid and dashed lines show the electron wavefunction with and without radiation, respectively.

that the MPGE's sign inversion takes place for an about 4 nm broader QW than the inversion of the g^* factor.³² The explanation of this fact requires an additional spin-independent orbital contribution to the MPGE, recently addressed by Tarasenko.¹⁵

A process resulting in the orbital linear MPGE is illustrated in Fig. 7. Here, we consider the in-plane motion of carriers subjected to the high-frequency electric field (e.g., THz radiation) applied along the x direction and an in-plane magnetic field along the y direction. For linearly polarized radiation, the electric field $\mathbf{E}(t)$ leads to a back and forth motion of electrons with velocity $\mathbf{v}(t)$ as illustrated in Fig. 7 for two different times. Without external field the electron's wave function is localized closer to one interface due to the asymmetrical doping, and its momentum relaxation rate $1/\tau_p$ has a contribution controlled by scattering by this interface. The orbital MPGE originates from the combined action of electric and magnetic fields, described in the following. If $\mathbf{E}(t)$ is applied, at a certain time t_1 , the electron is accelerated by the in-plane ac electric field along the negative x direction. At the same time, the electron with velocity v_x is subjected to the magnetic field B_y . This results in the Lorentz force $\mathbf{F}_L = e(\mathbf{v} \times \mathbf{B})$ which shifts the wave function to the center of the quantum well and thus decreases the scattering probability (see Fig. 7). Half a period later, at $t_2 = t_1 + T/2$, the electron velocity gets reversed so that the direction of the Lorentz force reverses as well. Now, the electron wave function is pushed closer to the interface, which increases the scattering rate and decreases the momentum relaxation. The resulting imbalance of the relaxation times for the motion along positive and negative x direction causes a net electric current proportional to the magnetic field strength. Obviously this mechanism yields a photocurrent, which does not change its sign with a variation of the QW width. Microscopically, the orbital contribution to the linear MPGE current $\mathbf{j}_{\text{orb}}^L$ is caused by the effect of a magnetic field on the scattering. The in-plane magnetic field results in a \mathbf{k} -dependent mixing of the eigenstates ϕ_1 and ϕ_2 , and the envelope in the ground subband becomes $k_\alpha B_\beta$ -dependent¹⁵

$$\psi_{1\mathbf{k}}(z) = \phi_1(z) + (\mathbf{k} \times \mathbf{B})_z \frac{e\hbar}{m} \frac{z_{21}}{E_{21}} \phi_2(z). \quad (6)$$

This leads to the following contribution in the scattering

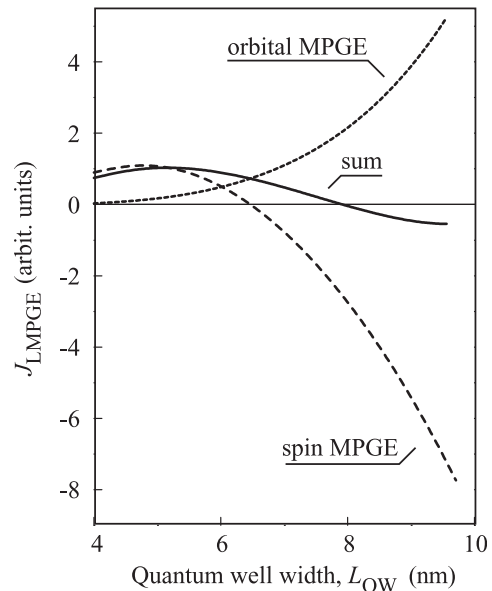


FIG. 8: Dependence of the spin-dependent (triangles) and orbital (squares) contributions to MPGE on QW width.

probability

$$W_{\mathbf{k}'\mathbf{k}} = W_0 \{1 + \zeta [\mathbf{B} \times (\mathbf{k} + \mathbf{k}')_z]\}, \quad (7)$$

where the parameter ζ is caused by SIA. The dependence $\zeta(L_{\text{QW}})$ determines the dependence of $\mathbf{j}_{\text{orb}}^L$ on the quantum well width yielding

$$\mathbf{j}_{\text{orb}}^L(L_{\text{QW}}) \sim \left(\frac{z_{21}}{E_{21}}\right)^2. \quad (8)$$

The quadratic dependence on the parameter z_{21}/E_{21} appears because, both, the electric field of the impurities and the magnetic field, lead to a mixing of the ground and first excited levels, Eqs. (4) and (6). Here, like for Eq. (5), we also assume that additional factors originating from the scattering asymmetry depend weakly on the QW width.

On the phenomenological level both mechanisms are described by the same equations and the total current is given by the sum of both contributions

$$\mathbf{j}^L = \mathbf{j}_{\text{spin}}^L + \mathbf{j}_{\text{orb}}^L. \quad (9)$$

The phenomenological similarity hinders the decomposition of both terms, because the spin contribution $\mathbf{j}_{\text{spin}}^L$ and the orbital one $\mathbf{j}_{\text{orb}}^L$ behave identically under a variation of the radiation's polarization state and the orientation of the magnetic field relative to the crystallographic axes. Our above consideration shows, however, that the behavior of the photocurrent upon a variation of the QW width allows us to distinguish between these two basically different mechanisms. The observed sign inversion clearly demonstrates that the total current almost reflects the behavior of the g^* factor and, therefore, is

in most samples dominated by the spin mechanism. The small shift of the MPGE's inversion point to a larger L_{QW} compared to the one of the g^* factor, however, demonstrates that the orbital MPGE also contributes and its magnitude is smaller but still comparable to that of the spin MPGE. For a QW with L_{QW} of about 6.5 nm the g^* factor is equal to zero and the MPGE is solely caused by the orbital mechanism.

The dependence of j_{orb}^L on the quantum well width, calculated after Eq. (8) is plotted in Fig. 8. Figure 8 shows that this current rises with increasing L_{QW} due to the increase of the mixing parameter z_{21}/E_{21} with L_{QW} but does not change its sign. This behavior is explained as follows: In narrow QWs the electric and magnetic fields can not efficiently mix size-quantized states because of their large energy separation E_{21} . In wider QWs the confinement is weaker, and the photocurrent increases. This strong dependence is valid for not too wide QWs, where only the ground subband is occupied. In very wide QWs, the photocurrent dependence on the QW width has a maximum and then the photocurrent tends to zero since in bulk GaAs photogalvanic effects are absent.

Figure 8 also shows the interplay of both contributions. To obtain this curve, we have normalized both contributions in such a way that the total current vanishes for the QW width where the photocurrent's sign inversion has been detected. One can see that the total photocurrent vanishes for a larger QW width than the g^* factor. This is due to the orbital contribution.

V. CIRCULAR MPGE

The sign inversion upon a variation of the QW width is also obtained for the SIA-induced circular MPGE. Figure 9 shows the helicity dependence of the photocurrent J_x , which clearly demonstrates the fingerprint of the circular MPGE: The sign inversion upon switching the radiation's helicity P_{circ} from +1 to -1 at $\varphi = 45^\circ$ (σ^+) and $\varphi = 135^\circ$ (σ^-), respectively. We note, that the whole polarization dependence stems from the interplay of the circular and linear MPGE. In agreement with the phenomenological theory³⁵ the signal can be well fitted by $J_x = AP_{\text{circ}} + B(1 + \cos 4\varphi) + C \sin 4\varphi$. Here the first term, given by the parameter A , is due to the circular MPGE and the following two, proportional to the coefficients B and C , stem from the linear MPGE discussed above and vanish for circularly polarized radiation. Figure 10 shows the quantum well width dependence of the circular photocurrent. In order to extract the circular MPGE from the total current and to ensure that no spurious currents contribute to the signal we used the fact that the circular MPGE reverses its sign upon switching the radiation's helicity from +1 (σ^+) to -1 (σ^-) and obtain the circular photocurrent after

$$J_x^C = [J_x(\sigma^+) - J_x(\sigma^-)]/2, \quad (10)$$

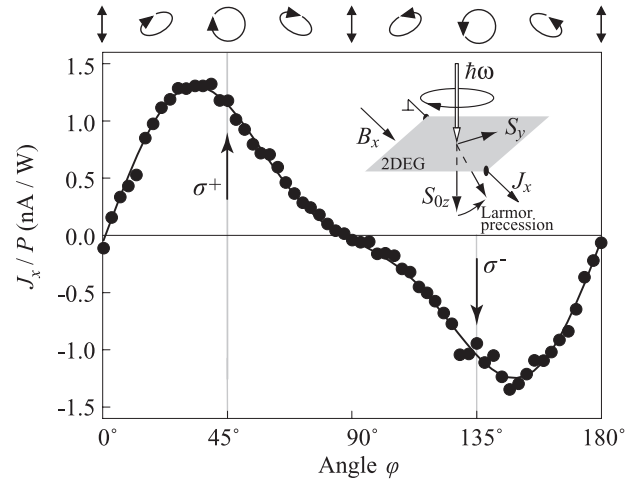


FIG. 9: Helicity dependence of the MPGE obtained for sample A at room temperature, $|\mathbf{B}| = 1$ T and a photon energy of $\hbar\omega = 4.4$ meV. The ellipses on top illustrate the polarization states for various angles of the $\lambda/4$ plate, φ . The inset depicts the spin-galvanic effect.

where $J_x(\sigma^+)$ and $J_x(\sigma^-)$ are photocurrents measured at σ^+ - and σ^- -polarized excitation. Because the circular MPGE also reverses its sign upon the inversion of the magnetic field direction, the current after Eq. (10) is further treated similarly to the linear MPGE according to Eq. (2). For the circular MPGE, we also observed that the photocurrent reverses its sign at a certain QW width.³⁶ Similarly to the behavior of the linear MPGE, the sign inversion of the photocurrent in Fig. 10 does not coincide with that of the Landé factor and takes place at $L_{\text{QW}} \sim 15$ nm. We show below that, similarly to the linear MPGE discussed earlier, this fact indicates the interplay of the spin and orbital mechanisms in the circular MPGE.

The spin mechanism of the circular MPGE is based on the spin-galvanic effect.¹² This effect results in the generation of an electric current due to a non-equilibrium spin polarization and is caused by its asymmetric spin relaxation. The spin-galvanic current and the average non-equilibrium spin \mathbf{S} are related by a second rank pseudotensor, with components proportional to the parameters of the spin-orbit splitting, as follows

$$j_{\text{spin},\alpha}^C = \sum_{\gamma} Q_{\alpha\gamma} S_{\gamma}. \quad (11)$$

For (001)-grown zinc-blende structure based QWs of C_{2v} -symmetry, the spin-galvanic effect is allowed only for a spin polarized electron gas with spins oriented in the QW plane. In the coordinate system parallel to the cubic axes, Eq. (11) reduces to $j_x^{\text{SIA}} = Q_{xy} S_y$ and $j_y^{\text{BIA}} = Q_{yy} S_y$, with j_x^{SIA} and j_y^{BIA} proportional to the Rashba and the Dresselhaus constants, respectively.²⁴ The spin-galvanic effect generally does not require optical excitation. In fact, the non-equilibrium spin can be achieved by both

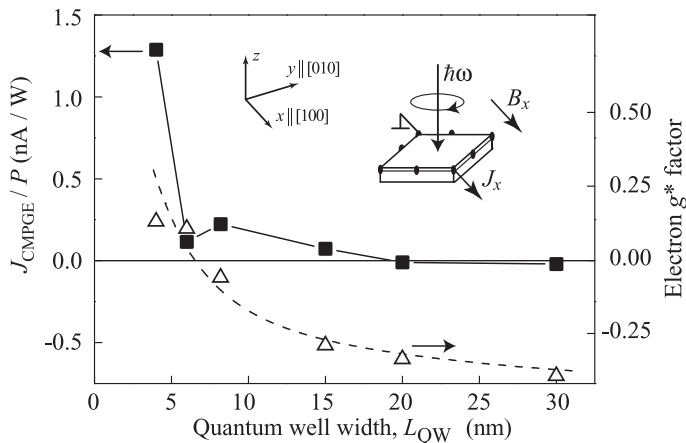


FIG. 10: Dependence of the circular MPGE (squares) on L_{QW} obtained at room temperature, $|\mathbf{B}| = 1$ T and a photon energy of $\hbar\omega = 4.4$ meV and corresponding g^* factors (triangles, by TRKR). The inset shows the experimental geometry for the CMPGE.

optical and non-optical methods, e.g., by electrical spin injection.

The spin-dependent contribution $\mathbf{j}_{\text{spin}}^{\text{C}}$ stems from the asymmetry in the spin relaxation, arising due to the Rashba spin-orbit splitting of the electronic ground subband and being linear in the in-plane wave vector \mathbf{k} :

$$E_{1\uparrow} - E_{1\downarrow} = \hbar\Omega. \quad (12)$$

Here the SIA-induced \mathbf{k} -linear spin-orbit splitting $\hbar\Omega$ is measured by TRKR technique, Sec. III.

An optical method, which provides a non-equal population of an uniform distribution in both spin subbands was proposed in Ref. 12. This method, sketched in the inset of Fig. 9, is based on the optical excitation with circularly polarized light yielding a steady-state spin orientation S_{0z} in the growth direction. The in-plane magnetic field then rotates, due to the Larmor precession, the optically oriented spins into the plane of the 2DES. If \mathbf{B} is oriented along the x axis we obtain a non-equilibrium spin polarization S_y which reads after time averaging¹²

$$S_y = -\frac{\omega_L \tau_{s\perp}}{1 + (\omega_L \tau_s)^2} S_{0z}, \quad (13)$$

where $\tau_s = \sqrt{\tau_{s\parallel} \tau_{s\perp}}$ and $\tau_{s\parallel}, \tau_{s\perp}$ are the longitudinal and transverse electron spin relaxation times, the Larmor frequency is given by $\omega_L = g^* \mu_B B_x / \hbar$, μ_B is the Bohr magneton, and $S_{0z} = \tau_{s\parallel} \dot{S}_z$ is the steady state electron spin polarization in the absence of a magnetic field. According to Eq. (11) the in-plane spin polarization S_y causes a net electric current in the direction along the magnetic field. For the investigated QWs at room temperature $\omega_L \tau_s \ll 1$ and, therefore, the photocurrent is proportional to $g^* B_y$.

The QW width dependence of $\mathbf{j}_{\text{spin}}^{\text{C}}$ is given by

$$\mathbf{j}_{\text{spin}}^{\text{C}}(L_{\text{QW}}) \sim g^*(L_{\text{QW}}) \Omega(L_{\text{QW}}) \tau_s^2(L_{\text{QW}}). \quad (14)$$

Equation (14) shows that this contribution is proportional to the g^* factor and, consequently, reflects its behavior upon a QW width variation.³⁸ Despite the QW width dependence of $\mathbf{j}_{\text{spin}}^{\text{C}}$ does not coincide with $g^*(L_{\text{QW}})$, this contribution to the photocurrent vanishes in QWs with $g^* = 0$. The fact that in GaAs/AlGaAs QWs the current, similarly to the g^* factor, changes its sign upon a variation of L_{QW} qualitatively explains the MPGE's sign inversion but can not clarify the difference in the two zero points. To explain this shift we should again address the possible contribution of the orbital MPGE.

An orbital mechanism yielding a helicity driven MPGE current was recently suggested in Ref. 16 and is given by

$$\mathbf{j}_{\text{orb},\alpha}^{\text{C}} = P_{\text{circ}} |E_0|^2 \sum_{\gamma} R_{\alpha\gamma} B_{\gamma}. \quad (15)$$

The second rank pseudotensor \mathbf{R} has the same space symmetry properties as the pseudotensor \mathbf{Q} , describing the spin-galvanic effect. However, the tensor \mathbf{R} is invariant under time inversion. Microscopically, the orbital contribution to the circular MPGE appears similarly to the one to the linear MPGE current described above. The current is caused by the action of the Lorentz force on the orbital motion of the 2D electrons in the radiation field. Under irradiation with circularly polarized light electrons perform a cyclic motion and, due to SIA, the presence of an in-plane magnetic field forces them to flow predominantly along the direction of \mathbf{B} . Reversing the radiation's helicity, changes the current direction. The microscopic theory of this effect is given in Ref. 16. The resulting current $\mathbf{j}_{\text{orb}}^{\text{C}}$, is caused by the \mathbf{B} -dependent corrections to the scattering probability, Eq. (7), as well as the corresponding contribution to the linear MPGE. The photocurrents due to the circular and linear MPGE are linked to each other according to $\mathbf{j}_{\text{orb}}^{\text{C}} \sim \mathbf{j}_{\text{orb}}^{\text{L}} \omega \tau_p$ at $\omega \tau_p \ll 1$ (Ref. 15). Using Eq. (8), we can, consequently, estimate the QW width dependence of $\mathbf{j}_{\text{orb}}^{\text{C}}$ as

$$\mathbf{j}_{\text{orb}}^{\text{C}}(L_{\text{QW}}) \sim \left(\frac{z_{21}}{E_{21}} \right)^2. \quad (16)$$

This equation shows that the orbital contribution to the circular MPGE has a constant-sign dependence on the QW width. Thus, the observed sign inversion of the circular MPGE and the shift between its zero crossing and that of the g^* factor agrees with the picture of the interplay of comparable spin and orbital contributions to this phenomenon.

Both mechanisms of the circular MPGE contribute to the total current $\mathbf{j}^{\text{C}} = \mathbf{j}_{\text{spin}}^{\text{C}} + \mathbf{j}_{\text{orb}}^{\text{C}}$ and are described phenomenologically by similar equations. The observed sign inversion proves that, in correspondence with the results of the linear MPGE, the dominant contribution comes from the spin-galvanic effect. While the spin-galvanic effect dominates the current for most of the investigated samples, the existence of the orbital circular MPGE is also clearly demonstrated. In particular, for QWs with a

width of about 6.5 nm the spin-galvanic effect vanishes and the current is caused solely by the orbital circular MPGE.

VI. SUMMARY

To summarize, our experiments clearly demonstrate that, both, linear and circular MPGE in GaAs/AlGaAs QW structures result from spin and orbital contributions. Our experiments show that for most quantum well widths the MPGE is mainly driven by spin-related mechanisms, which result in a photocurrent proportional to the g^* factor. For structures with a vanishingly small g^* factor, however, the MPGE caused by orbital mechanisms is clearly observed. Our work demonstrates that a varia-

tion of the electron g^* factor by different means, like varying the QW width, as it is done here, doping with magnetic impurities or using narrow band materials, where g^* and the spin-orbit interaction are enhanced, can be used for the separation of these qualitatively different mechanisms. Moreover, the orbital MPGE can be studied independently in materials with a vanishingly small spin-orbit interaction, like Si-based metal-oxide-semiconductor low dimensional structures.

We thank S.A. Tarasenko and E.L. Ivchenko for fruitful discussions and support, as well as M. Schmalzbauer. This work is supported by the DFG via programs SPP 1285, SFB 689, by the Linkage Grant of IB of BMBF at DLR, Russian Ministry of Education and Sciences, RFBR and “Dynasty” foundation — ICFPM.

-
- ¹ L. D. Landau and E. M. Lifshits, Course of theoretical physics V “Statistical Physics”.
- ² *Excitons*, edited by E. I. Rashba and M. D. Sturge (North-Holland, Amsterdam, 1982).
- ³ J. Fabian, A. Matos-Abiague, C. Ertler, P. Stano, and I. Zutic, *Acta Physica Slovaca* **57**, 565 (2007), arXiv:cond-mat/0711.1461.
- ⁴ E.L. Ivchenko, *Optical Spectroscopy of Semiconductor Nanostructures* (Alpha Science Int., Harrow, UK, 2005).
- ⁵ S. D. Ganichev and W. Prettl, *Intense Terahertz Excitation of Semiconductors* (Oxford University Press, Oxford 2006).
- ⁶ R. Winkler, *Spin-Dependent Transport of Carriers in Semiconductors*, in *Handbook of Magnetism and Advanced Magnetic Materials* (John Wiley & Sons, NY 2007); ibido arXiv cond-mat: 0605390 (2006).
- ⁷ E. L. Ivchenko and S. D. Ganichev, *Spin Photogalvanics in Spin Physics in Semiconductors*, edited by M. I. D’yakonov (Springer, Berlin 2008).
- ⁸ V. V. Bel’kov and S. D. Ganichev, *Semicond. Sci. Technol.* **23**, 114003 (2008).
- ⁹ V. V. Bel’kov and S. D. Ganichev, *Zero-bias spin separation*, in *Handbook of Spintronic Semiconductors*, edited by W. M. Chen and I. A. Buyanova (Pan Stanford Publishing, Singapore 2010).
- ¹⁰ S. D. Ganichev, V. V. Bel’kov, S. A. Tarasenko, S. N. Danilov, S. Giglberger, C. Hoffmann, E. L. Ivchenko, D. Weiss, W. Wegscheider, C. Gerl, D. Schuh, J. Stahl, J. de Boek, G. Borghs and W. Prettl, *Nature Physics* **2**, 609 (2006).
- ¹¹ V. V. Bel’kov, P. Olbrich, S. A. Tarasenko, D. Schuh, W. Wegscheider, T. Korn, C. Schüller, D. Weiss, W. Prettl, and S. D. Ganichev, *Phys. Rev. Lett.* **100**, 176806 (2008).
- ¹² S. D. Ganichev, E. L. Ivchenko, V. V. Bel’kov, S. A. Tarasenko, M. Sollinger, D. Weiss, W. Wegscheider, and W. Prettl, *Nature* **417**, 153 (2002).
- ¹³ S. D. Ganichev, Petra Schneider, V. V. Bel’kov, E. L. Ivchenko, S. A. Tarasenko, W. Wegscheider, D. Weiss, D. Schuh, B. N. Murdin, P. J. Phillips, C. R. Pidgeon, D. G. Clarke, M. Merrick, P. Murzyn, E. V. Bereguhin, and W. Prettl, *Phys. Rev. B* **68**, 081302 (2003).
- ¹⁴ S. D. Ganichev and W. Prettl, *J. Phys.: Condens. Matter* **15**, R935 (2003).
- ¹⁵ S. A. Tarasenko, *Phys. Rev. B* **77**, 085328 (2008).
- ¹⁶ S. A. Tarasenko, arXiv cond-mat: 1009.0681v1 (2010).
- ¹⁷ *Spin Physics in Semiconductors*, edited by M. I. Dyakonov (Springer, Berlin 2008).
- ¹⁸ *Semiconductor Spintronics and Quantum Computation* eds. D. D. Awschalom, D. Loss, and N. Samarth (Springer, Berlin 2010).
- ¹⁹ M. W. Wu, J. H. Jiang, and M. Q. Weng, *Phys. Reports* **493**, 61 (2010).
- ²⁰ M. J. Snelling, G. P. Flinn, A. S. Plaut, R. T. Harley, A. C. Tropper, R. Eccleston, and C. C. Phillips, *Phys. Rev. B* **44**, 11345 (1991).
- ²¹ E. L. Ivchenko, A. A. Kiselev, and M. Willander, *Sol. St. Com.* **102**, 375 (1997).
- ²² I. A. Yugova, A. Greilich, D. R. Yakovlev, A. A. Kiselev, M. Bayer, V. V. Petrov, Yu. K. Dolgikh, D. Reuter, and A. D. Wieck, *Phys. Rev. B* **75**, 245302 (2007).
- ²³ S. D. Ganichev, S. A. Emel’yanov, and I. D. Yaroshetskii, *Sov. Phys. JETP Lett.* **35**, 368 (1982).
- ²⁴ S. Giglberger, L. E. Golub, V. V. Bel’kov, S. N. Danilov, D. Schuh, Ch. Gerl, F. Rohlfing, J. Stahl, W. Wegscheider, D. Weiss, W. Prettl, and S. D. Ganichev, *Phys. Rev. B* **75** 035327 (2007).
- ²⁵ V. Lechner, L. E. Golub, P. Olbrich, S. Stachel, D. Schuh, W. Wegscheider, V. V. Bel’kov, and S. D. Ganichev, *Appl. Phys. Lett.* **94**, 242109 (2009).
- ²⁶ W. J. H. Leyland, G. H. John, R. T. Harley, M. M. Glazov, E. L. Ivchenko, D. A. Ritchie, I. Farrer, A. J. Shields, and M. Henini, *Phys. Rev. B* **75**, 165309 (2007).
- ²⁷ C. L. Yang, J. Dai, W. K. Ge, and X. Cui, *Appl. Phys. Lett.* **96**, 152109 (2010).
- ²⁸ M. I. Dyakonov and V. I. Perel, *Sov. Phys. - JETP* **33**, 1053 (1971).
- ²⁹ E. A. de Andrada e Silva, G. C. La Rocca, and F. Bassani, *Phys. Rev. B* **55**, 16293 (1997).
- ³⁰ Note, that χ of the sample with $L_{\text{QW}} = 4$ nm is twice as large as in the other samples, therefore SIA and consequently the SIA-induced current is enhanced compared to the samples with larger L_{QW} .
- ³¹ C. Drexler, V. V. Bel’kov, B. Ashkinadze, P. Olbrich, C. Zoth, V. Lechner, Ya. V. Terent’ev, D. R. Yakovlev, G.

- Karczewski, T. Wojtowicz, D. Schuh, W. Wegscheider, and S. D. Ganichev, *Appl. Phys. Lett.* **97**, 182107 (2010).
- ³² Note, that comparing our MPGE data obtained at room temperature with the g^* -factor behavior measured at low temperatures, we do not consider the weak temperature dependence g^* -factor,^{33,34} which may result in a small shift of its zero crossing.
- ³³ M. Oestreich and W. W. Rühle, *Phys. Rev. Lett.* **74**, 2315 (1995).
- ³⁴ W. Zawadzki, P. Pfeffer, R. Bratschitsch, Z. Chen, S. T. Cundiff, B. N. Murdin, and C. R. Pidgeon, *Phys. Rev. B* **78**, 245203 (2008)
- ³⁵ V. V. Bel'kov, S. D. Ganichev, E. L. Ivchenko, S. A. Tarasenko, W. Weber, S. Giglberger, M. Olteanu, H.-P. Tranitz, S. N. Danilov, Petra Schneider, W. Wegscheider, D. Weiss, and W. Prettl, *J. Phys. C: Condens. Matter* **17**, 3405 (2005).
- ³⁶ Note, that, like in the discussed above case of the linear MPGE, the current in the 4 nm broad QW is enhanced due to the larger parameter χ compared to the other samples.
- ³⁷ Here and latter the calculations are limited to rather narrow quantum wells, for which only one subband is occupied. In a wider QWs other subbands should be taken into account which is out of scope of this paper.
- ³⁸ We note, that recently an additional possible root of the spin-galvanic effect has been addressed in Ref. 39. Instead of SGE due to band spin splitting considered in Ref. 12, it is based on the spin-dependent scattering given by Eq. (3). However, this mechanism also yields a contribution proportional to the Zeeman splitting and does not qualitatively change the discussion of the MPGE variation upon the QW width change.
- ³⁹ L. E. Golub, *Pis'ma v ZhETF* **85**, 479 (2007) [*JETP Lett.* **85**, 393 (2007)].